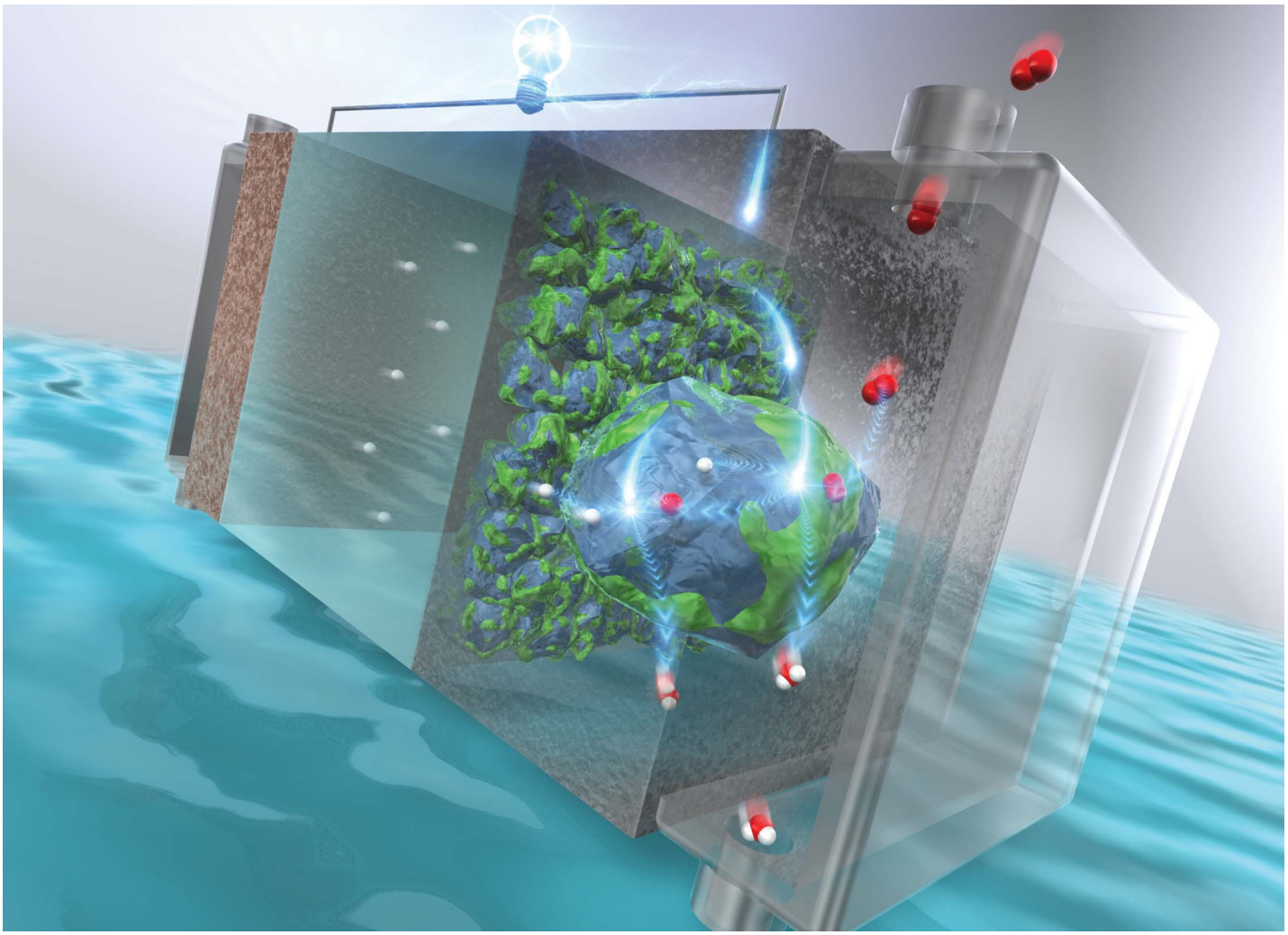

Highlighting a study on oxygen reduction reaction over composite cathodes for proton-conducting ceramic fuel cells by a group of researchers led by Dr. Toshiaki Matsui and Prof. Koichi Eguchi from Kyoto University, and Dr. Naoto Kamiuchi from Osaka University.

Oxygen reduction reaction over $(Ba,Sr)_6RE_2Co_4O_{15}$–$Ba(Ce,Pr,Y)O_3$ composite cathodes for proton-conducting ceramic fuel cells

The $(Ba,Sr)_6RE_2Co_4O_{15}$–$Ba(Ce,Pr,Y)O_3$ composites were developed for the cathode of proton-conducting ceramic fuel cells, and the mechanism of oxygen reduction reaction was investigated. We found that two reaction routes were promoted by in-situ surface modification of electrocatalysts through the elemental interdiffusion, resulting in high ORR activity: (1) the two phase boundary reaction, and (2) the dissociative adsorption of oxygen and the subsequent electrochemical reaction at the triple phase boundary.

As featured in:

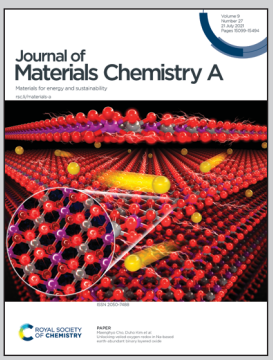

See Toshiaki Matsui *et al.*, *J. Mater. Chem. A*, 2021, **9**, 15199.

ROYAL SOCIETY OF CHEMISTRY

rsc.li/materials-a

Registered charity number: 207890

Journal of Materials Chemistry A

ROYAL SOCIETY OF CHEMISTRY

PAPER

View Article Online
View Journal | View Issue

Cite this: J. Mater. Chem. A, 2021, 9, 15199

Oxygen reduction reaction over $(Ba,Sr)_6RE_2Co_4O_{15}$–$Ba(Ce,Pr,Y)O_3$ composite cathodes for proton-conducting ceramic fuel cells†

Toshiaki Matsui, *[a] Naoki Kunimoto,[a] Kohei Manriki,[a] Kazunari Miyazaki,[a] Naoto Kamiuchi, [b] Hiroki Muroyama [a] and Koichi Eguchi[a]

Received 25th March 2021
Accepted 20th May 2021

DOI: 10.1039/d1ta02485j

rsc.li/materials-a

In this study, the effect of elemental substitution, especially the Ba/Sr ratio and rare-earth elements, in $(Ba,Sr)_6RE_2Co_4O_{15}$ (RE = La, Pr, Nd, Sm, Gd) and the composite effect with $BaCe_{0.5}Pr_{0.3}Y_{0.2}O_{3-\delta}$ on the activity for the oxygen reduction reaction were studied to develop high-performance cathodes for proton-conducting ceramic fuel cells. The polarization resistance of $(Ba_{6-x}Sr_x)RE_2Co_4O_{15}$ electrodes decreased with an increase in the Ba/Sr ratio, while the activity did not change systematically along the periodic table when the rare-earth element was substituted. Although the polarization resistance of $Ba_5SrGd_2Co_4O_{15}$ was about one order of magnitude lower than that of $Ba_4Sr_2Sm_2Co_4O_{15}$ at 500 °C, the composite of $Ba_5SrGd_2Co_4O_{15}$–$BaCe_{0.5}Pr_{0.3}Y_{0.2}O_{3-\delta}$ (30 : 70 wt%) exhibited comparable performance and activation energy to $Ba_4Sr_2Sm_2Co_4O_{15}$–$BaCe_{0.5}Pr_{0.3}Y_{0.2}O_{3-\delta}$ (30 : 70 wt%): polarization resistance – 0.20 Ω cm^2 and 0.52 Ω cm^2 at 600 °C and 500 °C, respectively, and activation energy – 61.8 kJ mol^{-1}. Then, the reason for the high performance of the $Ba_5SrGd_2Co_4O_{15}$–$BaCe_{0.5}Pr_{0.3}Y_{0.2}O_{3-\delta}$ (30 : 70 wt%) composite was studied in detail, especially from the viewpoint of elemental interdiffusion. Finally, the plausible oxygen reduction reaction mechanism on this composite was proposed.

Introduction

Proton-conducting ceramic fuel cells (PCFCs) have been attracting much attention due to the potential for achieving high energy conversion efficiency at intermediate temperatures, especially below 600 °C. This can be realized by the lower activation energy for the proton migration in proton-conducting oxides, such as acceptor-doped $BaCeO_3$ and $BaZrO_3$.[1–10] The avoidance of fuel dilution also contributes to enhancing the power output; this PCFC system can be operated at higher fuel utilization as compared to solid oxide fuel cells with oxide ion conductors since the steam is generated in the cathode. Recently, some groups have demonstrated remarkably high performance by applying novel materials and fabrication methods.[11–14] At the current state, however, the performance of PCFCs is mainly limited by the cathode activity;[11,15–17] it is required to develop a high-performance cathode with an area-specific resistance less than 0.1 Ω cm^2 at 600 °C.

Great efforts have been devoted to developing high performance PCFC cathodes.[18–26] The fabrication of composite electrodes consisting of a mixed oxide ion-electron conductor and a proton-conducting oxide is one of the promising approaches. In this case, a proton conductive electrolyte or a mixed proton–electron conductor is applied to introduce the proton conduction path, as well as to increase active reaction sites. Some oxides have also been reported to be triple-conducting materials, which allow simultaneous transport of protons, oxide ions, and electronic defects, *e.g.*, $BaCo_{0.4}Fe_{0.4}Zr_{0.1}Y_{0.1}O_{3-\delta}$ (ref. 11), $BaGd_{0.8}La_{0.2}Co_2O_{6-\delta}$ (ref. 27), and $Ba_{0.5}Sr_{0.5}Fe_{0.8}Zn_{0.2}O_{3-\delta}$ (ref. 28). Though some electrodes have been reported to have relatively high activity for the oxygen reduction reaction (ORR), sufficient durability and reliability have not been achieved yet.

Recently, we found that a new oxide of $Ba_4Sr_2Sm_2Co_4O_{15}$, which is one of the compounds of $(Ba_{6-x}Sr_x)RE_2Co_4O_{15}$ ($x = 1$, 2, RE = some rare-earth elements) (ref. 29) serves as an electrocatalyst for the ORR.[30] Furthermore, a remarkable composite effect was confirmed for the electrode based on the triple-conducting material of Pr and Y co-doped $BaCeO_3$ ($Ba(Ce,Pr,Y)O_{3-\delta}$) (ref. 31 and 22). In particular, the composite of $Ba_4Sr_2Sm_2Co_4O_{15}$–$BaCe_{0.5}Pr_{0.3}Y_{0.2}O_{3-\delta}$ (BSSC4224–BCPY) with a mixing ratio of 30 : 70 wt% exhibited higher activity below 600 °C in 3% humidified synthetic air, as compared with

[a]Department of Energy and Hydrocarbon Chemistry, Graduate School of Engineering, Kyoto University, Nishikyo-ku, Kyoto 615-8510, Japan. E-mail: matsui@elech.kuic.kyoto-u.ac.jp

[b]The Institute of Scientific and Industrial Research, Osaka University, 8-1 Mihogaoka, Ibaraki, Osaka 567-0047, Japan

† Electronic supplementary information (ESI) available: XRD patterns (Fig. S1 and S2), temperature dependence of area-specific resistance (Fig. S3), temperature dependence of total electrical conductivity (Fig. S4), temperature dependence of ohmic resistance (Fig. S5), SEM image (Fig. S6), and the result of EDS analysis (Table S1). See DOI: 10.1039/d1ta02485j

high-performance cathodes reported;[30] in this case, the volume ratio of BSSC4224 in this composite is almost the threshold value for the charge carrier conduction. Thus, it was suggested that the triple phase boundary of the BSSC4224/BCPY/gas phase is the electrochemically active reaction site and BSSC4224 serves as the active site for the dissociative adsorption of oxygen. However, the design guide for this composite system has not been established yet. It is required to verify the validity of the proposed electrode microstructure as well as the reaction mechanism. Moreover, this composite system has a potential to achieve higher ORR activity by modifying the chemical composition, optimizing the fabrication process, changing the mixing materials, *etc.* In this study, then, the effect of elemental substitution, especially the Ba/Sr ratio and rare-earth elements, in $(Ba,Sr)_6RE_2Co_4O_{15}$ and the composite effect with BCPY on the electrocatalytic activity were studied. We also focused on elemental interdiffusion in $(Ba,Sr)_6RE_2Co_4O_{15}$–$Ba(Ce,Pr,Y)O_3$ composites to clarify the reason for the high ORR activity.

Experimental

Powder preparation and characterization

The powders of $(Ba_{6-x}Sr_x)RE_2Co_4O_{15}$ ($x = 1$–3, RE = La, Pr, Nd, Sm, Gd), $BaCe_{0.5}Pr_{0.3}Y_{0.2}O_{3-\delta}$ (BCPY), $BaCe_{0.5-x}Co_xPr_{0.3}Y_{0.2}O_{3-\delta}$ (BCCPYx, x = 0.05–0.25), and $BaCe_{0.8}Y_{0.2}O_{3-\delta}$ (BCY) were synthesized by the Pechini method. Stoichiometric amounts of starting reagents were dissolved into distilled water: $Ba(NO_3)_2$ (Wako Pure Chemical Industries, Ltd.), $Sr(NO_3)_2$ (Wako Pure Chemical Industries, Ltd.), $Co(NO_3)_2\cdot 6H_2O$ (Wako Pure Chemical Industries, Ltd.), $Ce(NO_3)_3\cdot 6H_2O$ (Wako Pure Chemical Industries, Ltd.), $Pr(NO_3)_3\cdot 6H_2O$ (Sigma-Aldrich, Co.), $Y(NO_3)_3\cdot 6H_2O$ (Sigma-Aldrich, Co.), $Sm(NO_3)_3\cdot 6H_2O$ (Wako Pure Chemical Industries, Ltd.), $Gd(NO_3)_3\cdot 6H_2O$ (Wako Pure Chemical Industries, Ltd.), $Nd(NO_3)_3\cdot 6H_2O$ (Wako Pure Chemical Industries, Ltd.), and La $(NO_3)_3\cdot 6H_2O$ (Wako Pure Chemical Industries, Ltd.). Citric acid ($C_6H_8O_7\cdot H_2O$, Wako Pure Chemical Industries, Ltd.) and ethylene glycol (Wako Pure Chemical Industries, Ltd.) were added to the resulting solution at the molar ratio of citric acid/ethylene glycol/total metal cations of 1.5/1.5/1. The pH value of the solution was controlled to be *ca.* 8.0 with adding an aqueous ammonia solution (Wako Pure Chemical Industries, Ltd.). After that the solution was stirred at 80 °C until the water was evaporated. The obtained gel was pre-heated at 350 °C in air, and subsequently calcined at 1100 °C for 5 h in air. The crystal structures of resultant powders were identified by X-ray diffraction (XRD, Rigaku Ultima IV X-ray diffractometer, Cu Kα). The working conditions were 40 kV and 40 mA with a scanning rate of 20° min^{-1}. The diffraction patterns of $(Ba_{6-x}Sr_x)RE_2Co_4O_{15}$ ($x = 1$–3, RE = La, Pr, Nd, Sm, Gd) are summarized in Fig. S1 and S2 in the ESI.† The oxide powder of $Ba_5SrGd_2Co_4O_{15}$ (BSGC5124) was mixed with BCPY to form the composite, and subsequently annealed at 1000 °C for 5 h in air. After that, the local structure was analyzed using transmission electron microscopes (TEM), Tecnai G2 F20 (FEI Co.) and ARM-200F (JEOL Ltd.) equipped with an energy dispersive X-ray spectrometer (EDX, JED-2300).

Cell preparation

The symmetric cells consisting of various electrodes and a BCY disk electrolyte were fabricated as follows. The BCY powder was uniaxially pressed at 40 MPa into a pellet, followed by cold isostatic pressing at 300 MPa. The obtained pellet was fired at 1600 °C for 10 h in air, and subsequently polished to be 1 mm in thickness. The diameter of the pellet was *ca.* 19 mm. The relative density of the sintered BCY disk was higher than 98%. Some powders were mechanically mixed to form composites with varying the weight ratio. The slurries of electrodes were prepared by adding polyethylene glycol (molecular weight 400, Wako Pure Chemical Industries, Ltd.) to electrode powders. The slurry was screen-printed onto both sides of the BCY electrolyte, and then fired at 1000–1200 °C for 5 h in air. The diameter and thickness of the electrodes were 6 mm and *ca.* 20 μm, respectively. The electrode microstructure observation was performed by using a dual-beam focused ion beam-scanning electron microscope (FIB-SEM, NVision 40, Carl-Zeiss-SIINT) equipped with an EDX (Oxford).

Electrochemical measurements

The symmetrical cells were used to evaluate the ORR activity. The electrode performance was measured in 3 vol% humidified synthetic air (21% O_2–79% N_2) at 450–700 °C by impedance spectroscopy (CellTest system; potentiostat/galvanostat 1470E and frequency response analyzer 1455, Solartron Analytical, UK). The applied frequency was in the range of 0.1 Hz to 10^5 Hz with a voltage amplitude of 10 mV. The humidification was conducted by bubbling the gas through the water. Note that the electrode performance included the influence of the electronic leakage current because of the usage of symmetrical cells with a BCY electrolyte in the oxidizing atmosphere. However, the difference in the electrode performance obtained can be compared fairly. This is because the experimental conditions, such as the electrolyte thickness and the atmosphere, were fixed throughout this study. The electrode design concept obtained in this study can also be applied to cells using other electrolytes, such as $BaZrO_3$-based oxides.

Results and discussion

First of all, the effect of elemental substitution, especially the Ba/Sr ratio and rare-earth elements, in $(Ba,Sr)_6RE_2Co_4O_{15}$ on the ORR activity was studied. Fig. 1 shows impedance spectra at 550 °C and the temperature dependence of area-specific resistance (ASR) for $(Ba_{6-x}Sr_x)Sm_2Co_4O_{15}$ ($x = 1$–3) electrodes in 3 vol% humidified synthetic air. All oxides were fired on the BCY disk with a symmetrical configuration at 1200 °C. The polarization resistance decreased with an increase in the Ba/Sr ratio of $(Ba_{6-x}Sr_x)Sm_2Co_4O_{15}$, which was prominent below 650 °C. The same tendency was confirmed for $(Ba,Sr)_6Gd_2Co_4O_{15}$, as shown in Fig. S3.† Furthermore, the difference in the total electrical conductivity was confirmed; the conductivity for $Ba_5SrSm_2Co_4O_{15}$ was one order of magnitude higher or more than that for $Ba_3Sr_3Sm_2Co_4O_{15}$, as shown in Fig. S4.† These results indicate that the basicity, as well as the conductivity, strongly affects the

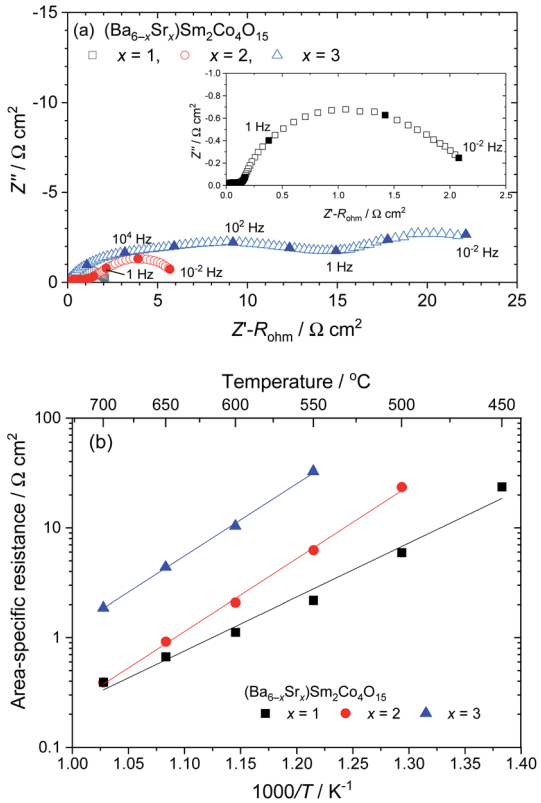

Fig. 1 (a) Impedance spectra at 550 °C and (b) temperature dependence of area-specific resistance for $(Ba_{6-x}Sr_x)Sm_2Co_4O_{15}$ ($x = 1, 2, 3$) electrodes in 3 vol% humidified synthetic air. All oxides were fired on the BCY disk at 1200 °C.

ORR activity; in other words, the material with higher basicity and electrical conductivity accelerates the ORR.

In Fig. 2, the influence of elemental substitution in the rare-earth site of $Ba_5SrRE_2Co_4O_{15}$ (RE = La, Pr, Nd, Sm, Gd) electrodes on the ORR activity was also studied. The activity did not

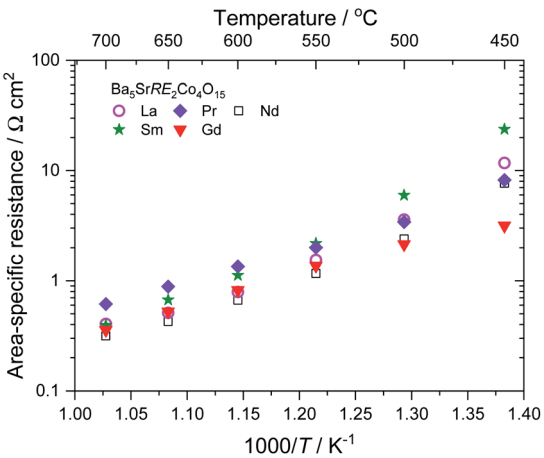

Fig. 2 Temperature dependence of area-specific resistance for $Ba_5SrRE_2Co_4O_{15}$ (RE = La, Pr, Nd, Sm, Gd) electrodes in 3 vol% humidified synthetic air at 450–700 °C. All oxides were fired on the BCY disk at 1200 °C.

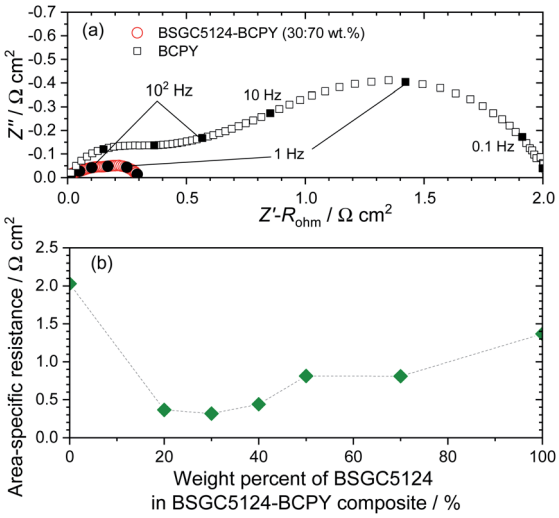

Fig. 3 (a) Impedance spectra of BSGC5124–BCPY (30 : 70 wt%) and BCPY electrodes and (b) area-specific resistance as a function of the weight percent of BSGC5124 in BSGC5124–BCPY composites at 550 °C in 3 vol% humidified synthetic air. Firing temperature of electrodes: 1000 °C for composites, 1100 °C for BCPY and 1200 °C for BSGC5124. BSGC5124 cannot be sintered to the electrolyte at 1000 °C but needs 1200 °C.

change systematically along the periodic table, and the remarkable elemental dependence on the ASR was not observed. At the current state, factors other than the basicity, which contributed to the activity, are unclear. Furthermore, it is apparent that the electrocatalytic activity of $(Ba_{6-x}Sr_x)RE_2Co_4O_{15}$ was insufficient for the practical use. Since

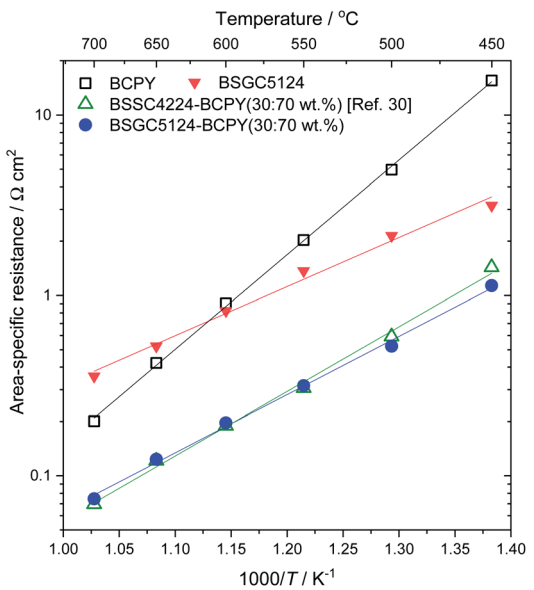

Fig. 4 Area-specific resistances of various electrodes as a function of reciprocal temperature in 3 vol% humidified synthetic air. Electrodes: BSGC5124, BSGC5124–BCPY (30 : 70 wt%), BCPY, and BSSC4224–BCPY (30 : 70 wt%) (ref. 30). In Fig. S5,† the temperature dependence of ohmic resistance for the symmetrical cell employing BSGC5124–BCPY (30 : 70 wt%) electrodes was plotted.

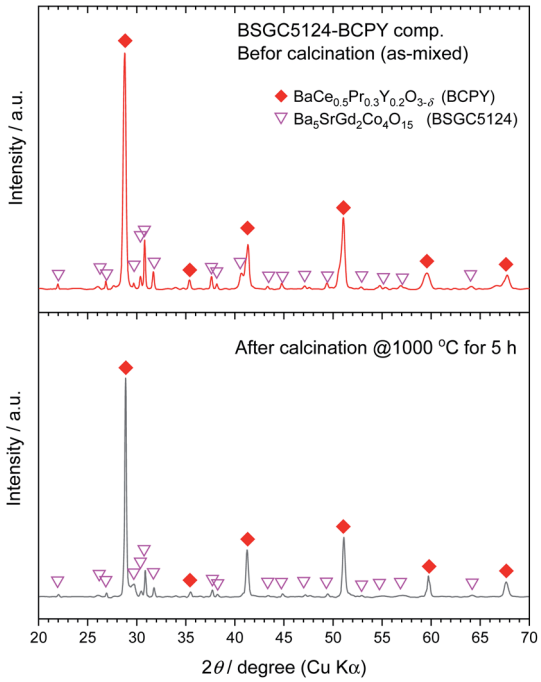

Fig. 5 XRD patterns of the BSGC5124–BCPY (30 : 70 wt%) composite before and after calcination at 1000 °C for 5 h in air.

$Ba_5SrGd_2Co_4O_{15}$ (BSGC5124) exhibited the lowest ASR with the lowest activation energy among electrodes studied, this material was applied for the composite electrodes with BCPY in the following part; note that BCPY was reported as a triple-conducting material.[22,31]

The composite electrodes of BSGC5124–BCPY were prepared by mixing two oxides with various weight ratios. Fig. 3(a) displays the impedance spectra of BSGC5124–BCPY (30 : 70 wt%) and BCPY electrodes. In Fig. 3(b), ASR as a function of the weight percent of BSGC5124 in the composites at 550 °C in 3 vol% humidified synthetic air is summarized. The composite effect was clearly observed in the mixing ratio of 20–40 wt% BSGC5124, and the BSGC5124–BCPY composite with a weight percent of 30 : 70 exhibited the lowest ASR. In the impedance spectra of these composites, a significant reduction in the low-frequency arc was confirmed as compared with that of BCPY. Since the weight ratio can be replaced almost equally to the volume ratio in this composite system, the volume ratio of BSGC5124, *ca.* 30%, is near the threshold for the charge carrier conduction, based on the percolation theory. This means that BSGC5124 did not serve as the main charge carrier conduction path. The ASR of BSGC5124–BCPY (30 : 70 wt%) as a function of reciprocal temperature in 3 vol% humidified synthetic air is presented in Fig. 4. For comparison, the results of BSGC5124, BCPY, and BSSC4224–BCPY (30 : 70 wt%) (ref. 30) are also plotted. Although the ASR of BSGC5124 was about one order of magnitude lower than that of BSSC4224 at 500 °C (see Fig. S3†), the performance of the BSGC5124–BCPY composite was almost comparable to that of BSSC4224–BCPY. Furthermore, both composites exhibited similar activation energy: BSGC5124–BCPY – 61.8 kJ mol^{-1}, BSGC4224–BCPY – 68.5 kJ mol^{-1}. Judging

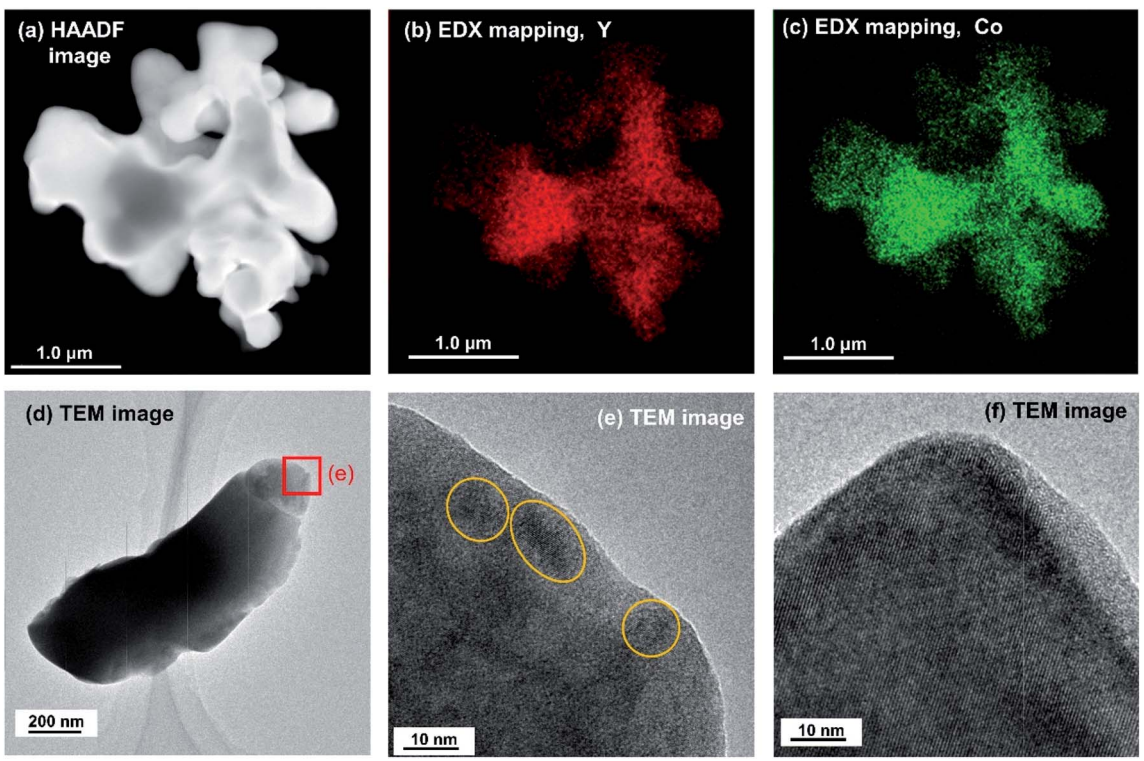

Fig. 6 TEM observation of BSGC5124–BCPY (30 : 70 wt%) composites calcined at 1000 °C for 5 h in air. (a) HAADF-STEM image of a typical particle, corresponding EDX maps of (b) Y and (c) Co elements, respectively, and (d)–(f) TEM images of other particles.

from the frequency response in impedance spectra and the activation energy, therefore, we can guess that BSGC5124 mainly serves as an active site for the dissociative adsorption of oxygen in the BSGC5124–BCPY composite, as in the case of the BSSC4224–BCPY composite.[30] In this case, the triple phase boundary of the BSGC5124/BCPY/gas phase is the main electrochemical reaction site.

In the following parts, the reason for the performance enhancement in the composite system was studied in detail. Fig. 5 shows the XRD patterns of BSGC5124–BCPY composites before and after calcination at 1000 °C for 5 h in air; this calcination condition is the same as that of the firing process of electrodes on the BCY disk. Although no impurity phase was formed after heat-treatment, a slight shift of diffraction patterns was confirmed for both oxides. This means that the elemental interdiffusion occurred during the heat-treatment. Then, TEM observation was performed for the composite powder to elucidate the local structure (see Fig. 6). The composite consisted of particles with a size from 500 nm to several μm as shown in Fig. 6(a) and (d). The EDX mapping revealed that Y and Co elements, derived from BCPY and BSGC5124, respectively, were present throughout the composite powder (Fig. 6(b) and (c)). Such elemental interdiffusion led to the peak shift in the XRD patterns in Fig. 5. The bulk of BCPY was highly crystalline in Fig. 6(f). In contrast, the amorphous layer was formed with a good wettability on the BCPY surface while including the crystallites with a size of 5–10 nm as indicated by the yellow circles in Fig. 6(e). This nanostructure of the amorphous layer including the crystallites will be derived from BSGC5124, since the same structure was confirmed for the powder of BSGC5124. In addition, the vulnerability of the surface oxide on BCPY to the electron beam irradiation during STEM-EDX analysis was also observed for the original BSGC5124 powder. Consequently, the local structure analysis has revealed that the BCPY phase is partially covered by the BSGC5124 phase, concomitant with the considerable elemental interdiffusion between two components. Such a surface modification will be one of the effective design strategies for PCFC cathodes.

In the next part, to clarify the impact of elemental interdiffusion on the ORR activity, the average composition of the BCPY phase after firing the composite electrode on the BCY disk was estimated by an SEM-EDX analysis (see Fig. S6 and Table S1†); it was impossible to distinguish two components from the cross-sectional SEM image of the BSGC5124–BCPY (30 : 70 wt%) composite. We found that the Co element diffusing from the BSGC5124 phase dissolved in the BCPY phase in the range of 1–3 mol%. Then, cobalt-containing BCPY of $BaCe_{0.5-x}Co_xPr_{0.3}Y_{0.2}O_{3-\delta}$ (BCCPYx, x = 0.05–0.25) was synthesized and their structural and electrochemical properties were investigated; note that only the Ce/Co ratio was varied with fixing the Pr and Y molar ratios to simplify the discussion. Fig. 7 shows the XRD patterns of BCPY and BCCPYx (x = 0.05–0.25). Only the diffraction patterns ascribable to the perovskite-structure were detected up to x = 0.15, while $BaCoO_3$-based oxide and CoO were formed as impurities at x = 0.2, 0.25. Thus, the powder was the mixture of BCCPY and impurities more than x = 0.2.

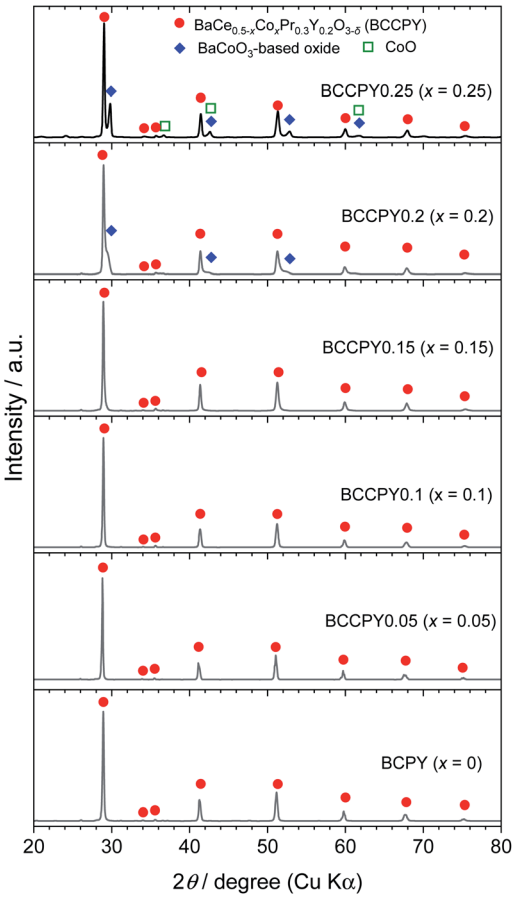

Fig. 7 XRD patterns of BCPY (x = 0) and $BaCe_{0.5-x}Co_xPr_{0.3}Y_{0.2}O_{3-\delta}$ (BCCPYx, x = 0.05–0.25).

According to the EDX analysis in Table S1,† the x value was in the range of 0.05–0.15 at each point in Fig. S6† with assuming the fixed Pr and Y molar ratios. Thus, the cobalt-containing BCPY phase in the composite electrode was within the single phase range. Fig. 8 displays the temperature dependence of ASR for BCPY and BCCPYx (x = 0.05–0.15) in 3 vol% humidified synthetic air and corresponding impedance spectra collected at 550 °C. Cobalt-containing BCPY exhibited almost the same or higher ORR activity as compared with BCPY. The ORR activity enhanced with an increase in the amount of cobalt up to x = 0.1, and then reduced at x = 0.15. It is clear from impedance spectra in Fig. 8(b) and (c) that the low frequency arc shrank significantly for BCCPY0.1, as compared with BCPY. The elementary processes related to the surface reaction, such as the dissociative adsorption of oxygen and the subsequent migration of adsorbed oxygen, will be mainly accelerated by the substitutional dissolution of cobalt. Interestingly, this spectral change also affected the activation energy; the activation energy of cobalt-containing BCPY was lower than that of the cobalt-free one. Thus, the rate limiting step is different depending on the presence or absence of the Co element. Consequently, the ORR at the two phase boundary of the BCCPYx/gas phase will be facilitated since pristine BCPY was reported as a triple-conducting material. In the case of BCPY0.15, the frequency

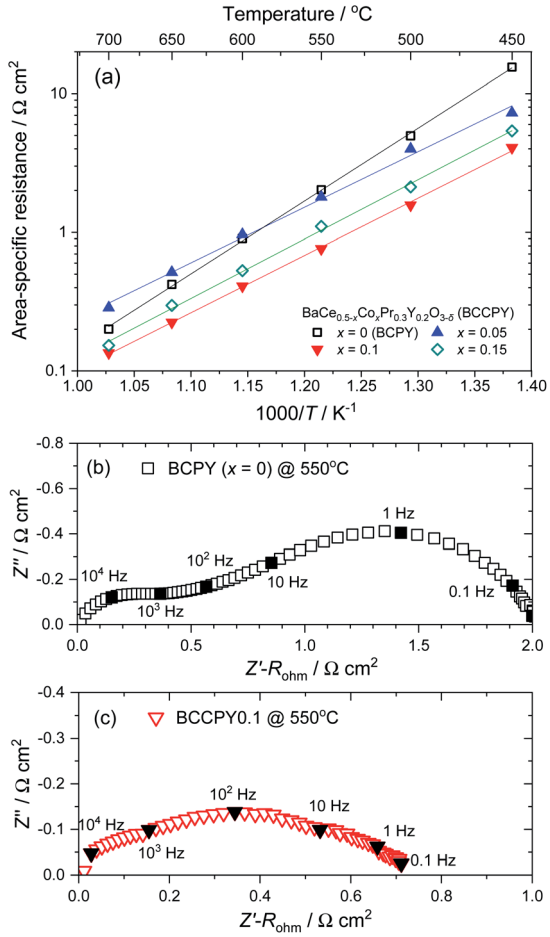

Fig. 8 (a) Temperature dependence of area-specific resistance for BCPY ($x = 0$) and $BaCe_{0.5-x}Co_xPr_{0.3}Y_{0.2}O_{3-\delta}$ (BCCPYx, $x = 0.05$–0.15) in 3 vol% humidified synthetic air and corresponding impedance spectra of (b) BCPY and (c) BCCPY0.1 electrodes at 550 °C. Firing temperature of electrodes: 1000 °C for BCCPYx ($x = 0.05$–0.15) and 1100 °C for BCPY.

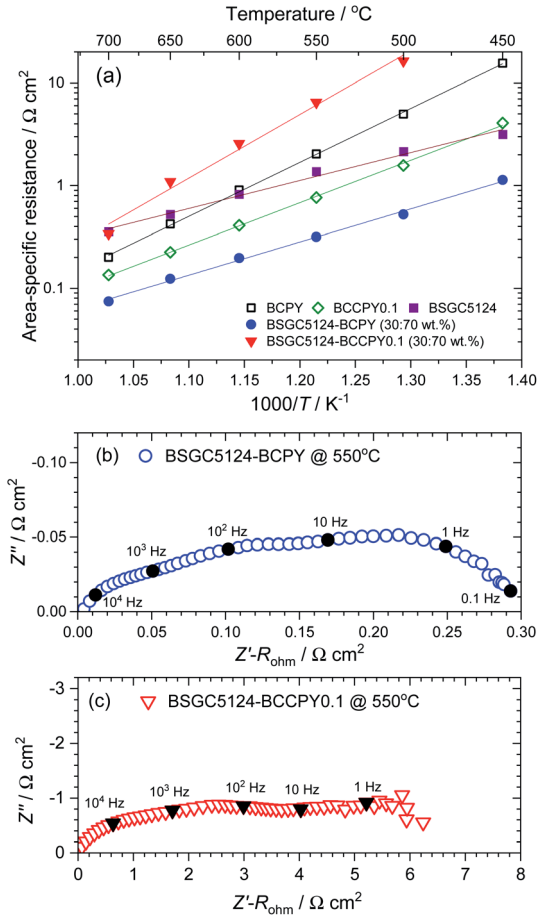

Fig. 9 (a) Temperature dependence of the area-specific resistance of BSGC5124–BCCPY0.1 (30 : 70 wt%) and BSGC5124–BCPY (30 : 70 wt%) electrodes in 3 vol% humidified synthetic air and corresponding impedance spectra of (b) BSGC5124–BCPY and (c) BSGC5124–BCCPY0.1 electrodes at 550 °C. Firing temperature of electrodes: 1000 °C for composites and BCCPY0.1, 1100 °C for BCPY and 1200 °C for BSGC5124.

response of the impedance spectrum was analogous to that of BCCPY0.1. The formation of small amounts of impurities may affect the ORR activity, considering the results in Fig. 7.

Since BCCPY0.1 exhibited the highest activity among the samples studied, this material was applied as the main electrical conduction component in the composite electrode. The temperature dependences of the area-specific resistance of BSGC5124–BCCPY0.1 (30 : 70 wt%) and BSGC5124–BCPY (30 : 70 wt%) composite electrodes in 3 vol% humidified synthetic air are shown in Fig. 9. Corresponding impedance spectra at 550 °C are also displayed. As described above, the mixing weight ratio can be almost equivalently converted to the volume ratio in the case of BSGC5124–BCPY. The same thing can be applied to the BSGC5124–BCCPY0.1 since the difference in the molecular weights between BCCPY0.1 and BCPY is less than 3%. Thus, the volume ratio of BSGC5124 in both composites is close to the threshold value for the charge carrier conduction through this phase, considering the percolation theory. Surprisingly, the drastic performance deterioration was confirmed for BSGC5124–BCCPY0.1 though BCCPY0.1 with the highest ORR activity was used. Furthermore, its activation energy also increased as compared with that of each constituent component, BSGC5124 and BCCPY0.1. This means that the distribution of cobalt in the composite decisively affected the ORR activity. The Co element comes out from BSGC5124 in this case, whereas a certain amount of cobalt already dissolved in BCCPY0.1. Thus, an excess amount of cobalt in BCCPY0.1 may lead to the formation of impurities such as $BaCoO_3$-based oxide, resulting in the reduction in the ORR activity of cobalt-containing BCPY as observed in Fig. 7 and 8. At the current state, however, the diffraction lines ascribable to impurities were not detected directly in an XRD analysis for BSGC5124–BCCPY0.1. The suppression of cobalt diffusion from BSGC5124 also inhibits the dissociative adsorption of oxygen over BSGC5124, judging from the impedance spectrum and activation energy. In other words, the formation of BSGC5124-derived oxide with a barium-rich surface induced by the cobalt diffusion will be an important factor to accelerate the dissociative adsorption of oxygen.

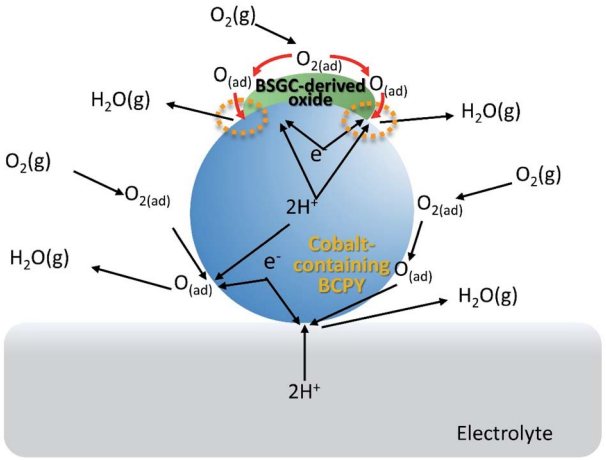

Fig. 10 Plausible ORR mechanism on the BSGC5124–BCPY (30 : 70 wt%) composite.

Summarizing the results and discussion so far, the plausible ORR mechanism on the BSGC5124–BCPY (30 : 70 wt%) composite can be drawn as shown in Fig. 10. BSGC5124-derived oxide partially covered the cobalt-containing BCPY surface with a good wettability; both phases were formed by elemental interdiffusion through the contacting interface. In this composite, two factors affect the electrocatalytic activity in a complex manner. Cobalt-containing BCPY is a mixed conductor and serves as ionic and electronic conduction paths. The enhancement in the ORR activity was confirmed concomitantly with the dissolution of cobalt cations into BCPY, leading to the promotion of the two phase boundary reaction. Furthermore, BSGC5124-derived oxide also played an important role in the ORR. The barium-rich surface with high activity for the dissociative adsorption of oxygen is formed accompanied by cobalt diffusion. In conclusion, we propose that *in situ* surface modification of electrocatalysts through elemental interdiffusion is one of the effective design strategies for PCFC cathodes. In this composite, however, the CO_2-resistivity of materials still remains as a drawback to be settled since the basicity is a trade-off relation with the ORR activity in CO_2-containing atmospheres.

Conclusions

The effect of elemental substitution in $(Ba,Sr)_6RE_2Co_4O_{15}$ on the ORR activity was studied, and we found that the basicity and the electrical conductivity were key factors. However, the order of the electrocatalytic activity of $(Ba,Sr)_6RE_2Co_4O_{15}$ was found to be not the same as that of composites with BCPY; the performance of the BSGC5124–BCPY (30 : 70 wt%) composite was almost comparable to that of BSSC4224–BCPY (30 : 70 wt%). The local structure analysis of BSGC5124–BCPY revealed that BSGC5124-derived oxide partially covered the surface of cobalt-containing BCPY with a good wettability because of the considerable elemental interdiffusion during the firing process. As a result, the promotion of two reaction routes resulted in high ORR activity in this composite: (1) the two phase boundary reaction over cobalt-containing BCPY, and (2) the dissociative adsorption of oxygen over BSGC5124-derived oxide and the subsequent electrochemical reaction at the triple phase boundary of the BSGC5124-derived oxide/cobalt-containing BCPY/gas phase. Therefore, *in situ* surface modification of electrocatalysts through elemental interdiffusion will be a good design guide to develop high-performance PCFC cathodes.

Conflicts of interest

There are no conflicts to declare.

Acknowledgements

This paper is partially based on results obtained from projects, Development of Ultra-High Efficiency Protonic Ceramic Fuel Cell Devices, WP1 Development of Innovative High-Performance Electrodes, JPNP20003, commissioned by the New Energy and Industrial Technology Development Organization (NEDO) and the research grant of the Toyota Mobility Foundation (TMF). TEM analysis in the present work was supported by "Dynamic Alliance for Open Innovation Bridging Human, Environment and Materials" from the Ministry of Education, Culture, Sports, Science and Technology (MEXT) of Japan.

References

1 H. Uchida, N. Maeda and H. Iwahara, *Solid State Ionics*, 1983, **11**, 117–124.
2 H. Iwahara, H. Uchida, K. Ono and K. Ogaki, *J. Electrochem. Soc.*, 1988, **135**, 529–533.
3 D. A. Stevenson, N. Jiang, R. M. Buchanan and F. E. G. Henn, *Solid State Ionics*, 1993, **62**, 279–285.
4 H. Iwahara, *Solid State Ionics*, 1996, **86–88**, 9–15.
5 R. C. T. Slade and N. Singh, *Solid State Ionics*, 1991, **46**, 111–115.
6 J. F. Liu and A. S. Nowick, *Solid State Ionics*, 1992, **50**, 131–138.
7 N. Bonanos, B. Ellis, K. S. Knight and M. N. Mahmood, *Solid State Ionics*, 1989, **35**, 179–188.
8 H. G. Bohn and T. Schober, *J. Am. Ceram. Soc.*, 2000, **83**, 768–772.
9 K.-D. Kreuer, *Annu. Rev. Mater. Res.*, 2003, **33**, 333–359.
10 M. Amsif, D. Marrero-Lopez, J. C. Ruiz-Morales, S. N. Savvin, M. Gabás and P. Nunez, *J. Power Sources*, 2011, **196**, 3461–3469.
11 C. Duan, J. Tong, M. Shang, S. Nikodemski, M. Sanders, S. Ricote, A. Almansoori and R. O'Hayre, *Science*, 2015, **349**, 1321–1326.
12 S. Choi, C. J. Kucharczyk, Y. G. Liang, X. H. Zhang, I. Takeuchi, H. I. Ji and S. M. Haile, *Nat. Energy*, 2018, **3**, 202–210.
13 K. Bae, D. Y. Jang, H. J. Choi, D. Kim, J. Hong, B.-K. Kim, J. H. Lee, J. W. Son and J. H. Shim, *Nat. Commun.*, 2017, **8**, 14553.

14 H. An, H. W. Lee, B. K. Kim, J. W. Son, K. J. Yoon, H. Kim, D. Shin, H. I. Ji and J. H. Lee, *Nat. Energy*, 2018, **3**, 870–875.
15 E. Fabbri, D. Pergolesi and E. Traversa, *Chem. Soc. Rev.*, 2010, **39**, 4355–4369.
16 L. Yang, S. Wang, X. Lou and M. Liu, *Int. J. Hydrogen Energy*, 2011, **36**, 2266–2270.
17 T. Onishi, D. Han, N. Hatada, Y. Noda, Y. Adachi, M. Majima and T. Uda, *J. Electrochem. Soc.*, 2015, **162**, F250–F257.
18 E. Fabbri, S. Licoccia, E. Traversa and E. D. Wachsman, *Fuel cells*, 2009, **9**, 128–138.
19 Y. Lin, R. Ran, Y. Zheng, Z. Shao, W. Jin, N. Xu and J. Ahn, *J. Power Sources*, 2008, **180**, 15–22.
20 H. Yamamura, T. Ikuta, H. Yahiro and G. Okada, *Solid State Ionics*, 2005, **176**, 269–274.
21 L. Yang, Z. Liu, S. Wang, Y. Choi, C. Zuo and M. Liu, *J. Power Sources*, 2010, **195**, 471–474.
22 L. Yang, C. Zuo, S. Wang, Z. Cheng and M. Liu, *Adv. Mater.*, 2008, **20**, 3280–3283.
23 E. Fabbri, I. Markus, L. Bi, D. Pergolesi and E. Traversa, *Solid State Ionics*, 2011, **202**, 30–35.
24 E. Fabbri, L. Bi, D. Pergolesi and E. Traversa, *Energy Environ. Sci.*, 2011, **4**, 4984–4993.
25 Y. Rao, S. Zhong, F. He, Z. Wang, R. Peng and Y. Lu, *Int. J. Hydrogen Energy*, 2012, **37**, 12522–12527.
26 L. Bi and E. Traversa, *J. Mater. Res.*, 2014, **29**, 1–15.
27 R. Strandbakke, V. A. Cherepanov, A. Y. Zuev, D. S. Tsvetkov, C. Argirusis, G. Sourkouni, S. Prünte and T. Norby, *Solid State Ionics*, 2015, **278**, 120–132.
28 D. Poetzsch, R. Merkle and J. Maier, *Phys. Chem. Chem. Phys.*, 2014, **16**, 16446–16453.
29 W. Wong-Ng, G. Liu, Y. G. Yan and J. A. Kaduk, *Powder Diffr.*, 2013, **28**, 212–221.
30 T. Matsui, K. Manriki, K. Miyazaki, H. Muroyama and K. Eguchi, *J. Mater. Chem. A*, 2018, **6**, 14188–14194.
31 C. Zuo, S. Zha, M. Liu, M. Hatano and M. Uchiyama, *Adv. Mater.*, 2006, **18**, 3318–3320.

